Available at www.sciencedirect.com

ScienceDirect

journal homepage: www.elsevier.com/locate/he

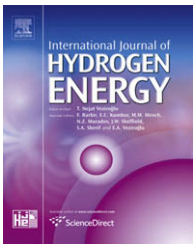

Measurements of laminar burning velocities and onset of cellular instabilities of methane–hydrogen–air flames at elevated pressures and temperatures

Erjiang Hu, Zuohua Huang, Jiajia He, Jianjun Zheng, Haiyan Miao*

State Key Laboratory of Multiphase Flow in Power Engineering, Xi'an Jiaotong University, 28 Xian Ning West Road, Xi'an 710049, Shaanxi Province, PR China

ARTICLE INFO

Article history:
Received 28 March 2009
Received in revised form
25 April 2009
Accepted 26 April 2009
Available online 4 June 2009

Keywords:
Methane
Hydrogen
Laminar burning velocity
Onset of cellular instability
Elevated pressures and temperatures

ABSTRACT

An experimental study on laminar burning velocities and onset of cellular instabilities of the premixed methane–hydrogen–air flames was conducted in a constant volume combustion vessel at elevated pressures and temperatures. The unstretched laminar burning velocity and Markstein length were obtained over a wide range of hydrogen fractions. Besides, the effects of hydrogen addition, initial pressure and initial temperature on flame instabilities were analyzed. The results show that the unstretched flame propagation speed and the unstretched laminar burning velocity are increased with the increase of initial temperature and hydrogen fraction, and they are decreased with the increase of initial pressure. Early onset of cellular instability is presented and the critical radius and Markstein length are decreased with the increase of initial pressure, indicating the increase of hydrodynamic instability with the increase of initial pressure. Flame instability is insensitive to initial temperature compared to initial pressure. With the increase of hydrogen fraction, significant decrease in critical radius and Markstein length is presented, indicating the increase in both diffusional-thermal and hydrodynamic instabilities as hydrogen fraction is increased.

1. Introduction

With increasing concern on fossil fuel shortage and stringent emission regulations, the development of alternative fuel engines has attracted more and more attention around the world. Natural gas, is a clean fuel in which methane is its major component, is considered to be one of the most favorable fuels for engines, and the utilization of natural gas has been realized in the spark-ignition engines. However, due to the slow burning velocity of natural gas and its poor lean-burn capability, the natural gas spark-ignition engine still has its disadvantages like low thermal efficiency, large cycle-by-cycle variation, and poor lean-burn capability, and these will decrease the engine power output and increase the fuel consumption [1,2]. One of the effective methods to solve the problem of slow burning velocity of natural gas is to mix natural gas with a fuel that possesses high burning velocity. Hydrogen is regarded as the best gaseous candidate due to its high burning velocity, and the combination of natural gas with hydrogen is expected to improve the lean-burn characteristics and decrease the engine emissions [3–8].

In order to understand the effect of hydrogen addition into natural gas on engine combustion, the understanding of

* *Corresponding author*. Tel.: +86 29 82665075; fax: +86 29 82668789.
E-mail address: zhhuang@mail.xjtu.edu.cn (Z. Huang).

0360-3199/$ – see front matter © 2009 International Association for Hydrogen Energy. Published by Elsevier Ltd. All rights reserved.
doi:10.1016/j.ijhydene.2009.04.058

fundamental combustion behavior with hydrogen enriched methane is indispensable. It will provide an in-depth understanding of combustion. Laminar burning velocity is the fundamental parameter in combustion and it is also the base parameter for turbulent burning velocity determination. Laminar burning velocity can be used to validate the chemical reaction mechanisms [9,10] and is of practical importance in the design and optimization of internal combustion engines and power plant burners [11]. There are three approaches to measure the laminar burning velocity, they are, the stagnation plane flame method [12,13], the heat flux method [14,15] and the combustion bomb method [16,17]. The stagnation plane flame method can establish different flame configurations, but it is difficult to draw a clear flame front and to stabilize the flame under the high-pressure conditions. With respect to the heat flux method, further work should be done to determine the heat loss as a function of inlet velocity and to extrapolate the results to zero heat loss to get the adiabatic burning velocity. The combustion bomb method utilizes the prototypical propagating spherical flame configuration and has drawn the particular attention due to its simple flame configuration, well-defined flame stretch rate and well-controlled experimentation [18,19]. Practically, the outwardly propagating flame is more similar to the flame propagation in the spark-ignition engines. In this study, the laminar burning velocities of methane–hydrogen–air mixtures were measured by using the spherically expanding flame.

Many previous researches on laminar burning velocities concentrated on the methane–air flames [13,16,18,20,21] and/or the hydrogen–air flames [9,19,22–26]. Recently, some experimental studies reported the measurement of laminar burning velocity for the methane–hydrogen–air flames [11,13,27–33]. Liu et al. [29] and Huang et al. [30] conducted more extensive experimental studies over a wide range of equivalence ratios and hydrogen fractions in the methane–hydrogen–air flames. Yu et al. [13] studied the laminar burning characteristics of methane–hydrogen–air flames with the assumption that the stoichiometrically small amounts of hydrogen in the mixture were completely consumed and found a linear correlation between laminar burning velocity and hydrogen fraction. Law and Kwon [27] studied the potential of hydrocarbon addition into hydrogen to suppress explosion hazards and found that a small or moderate amount of methane addition could remarkably reduce the laminar burning velocities and would suppress the propensity of onset of both diffusional-thermal instability and hydrodynamic cellular instability in hydrogen–air flames. However, these studies were mostly conducted at the atmospheric pressure and at the room temperature, and a few literatures on combustion of hydrogen enriched methane–air flames at elevated pressures and temperatures were reported.

As lean flames are likely to be unstable in both methane–air mixtures and hydrogen–air mixtures, lean combustion is widely used in engineering fields. Thus, this study will select the equivalence ratio of 0.8 to study the basic characteristics of the flames. The outwardly propagating spherical flame was used to obtain the laminar burning parameters, including the unstretched laminar burning velocity (u_l) and the burned gas Markstein length (L_b), which reflects the sensitivity of flame stability to flame stretch rate. In addition, the thermal expansion ratio (σ) and the laminar flame thickness (δ_l) of methane–hydrogen–air mixtures at elevated pressures and at different hydrogen fractions were provided to analyze the flame stability. Critical flame radius, Peclet number and influence of diffusional-thermal and hydrodynamic instabilities on the transition to cellular flames were analyzed. This study will provide further information and is beneficial in understanding methane–hydrogen–air mixture flames.

2. Experimental setup and procedures

Fig. 1 shows the experimental setup. It includes a constant volume combustion chamber and the systems for heating, ignition, data acquisition and high-speed Schlieren photography. The combustion chamber is a cylindrical type with an inner diameter of 180 mm and volume of 5.5 L as shown in Fig. 2. The centrally located electrodes are used to ignite the premixed mixtures. Pressure transmitter, thermocouple, pressure transducer, inlet and outlet valves are mounted on the chamber body. Two quartz windows with 80 mm diameter are located at the two sides of the vessel to allow an optical accessiblity. A high-speed digital camera (HG-100K) operating at 10,000 frames per second is used to record the flame photos during flame propagation. Fuel and dry air are supplied into the chamber through the inlet valve corresponding to the given equivalence ratio and dilution ratio. Five minutes is awaited before starting the ignition to ensure the homogeneity of methane–hydrogen–air mixtures.

In the experiments, the initial pressure is set at 0.1 MPa, 0.25 MPa, 0.5 MPa and 0.75 MPa and the initial temperature is set at 303 K, 373 K and 443 K, respectively. Hydrogen fractions are varied from 0% to 80%. Purities of methane and hydrogen in the study are 99.9% and 99.995%, respectively.

Hydrogen fraction (X_{H_2}) is defined as

$$X_{H_2} = \frac{V_{H_2}}{V_{CH_4} + V_{H_2}} \tag{1}$$

where V_{CH_4} and V_{H_2} are the volume fractions of methane and hydrogen in the fuel blends, respectively.

Total equivalence ratio (ϕ) is defined as

$$\phi = \frac{F/A}{(F/A)_{st}} \tag{2}$$

where F/A is the fuel–air ratio and $(F/A)_{st}$ refers to the stoichiometric value of F/A.

Mixture can be expressed as

$$\left(1 - X_{H_2}\right)CH_4 + X_{H_2}H_2 + \left(\frac{2}{\phi}(1 - X_{H_2})\frac{X_{H_2}}{2\phi}\right)(O_2 + 3.762N_2) \tag{3}$$

There are three reactants in the mixture, so it is necessary to define the stoichiometric parameters for data reduction. In the present work, the mole fractions of methane, hydrogen, fuel blend and air are n_{CH_4}, n_{H_2}, n_{Fuel}, and n_{Air}, respectively.

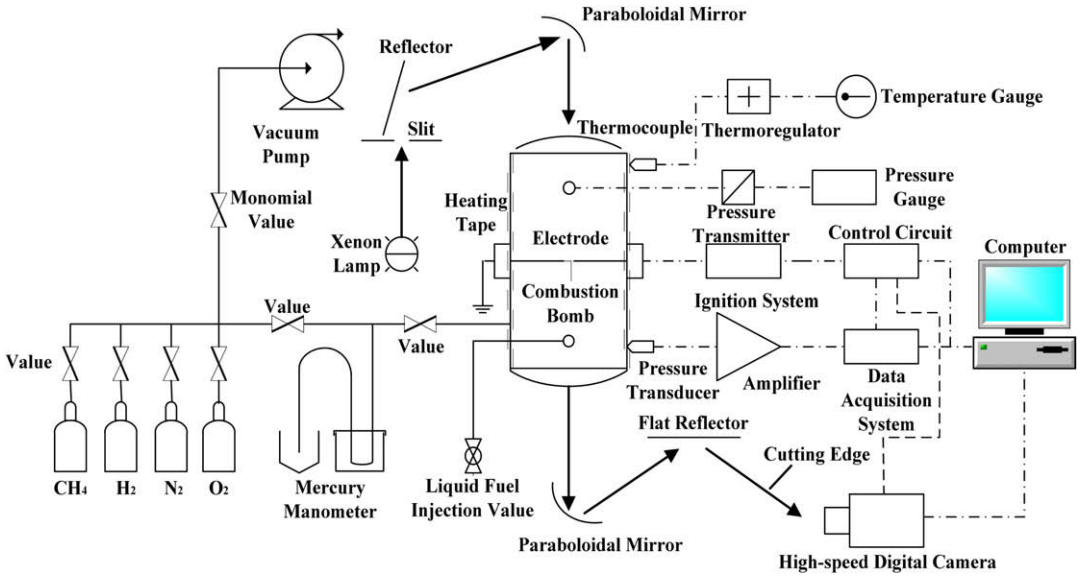

Fig. 1 – Experimental setup.

Thus, the hydrogen and methane based equivalence ratios are defined as

$$\phi_{H_2} = \frac{n_{H_2}/n_{Air}}{(n_{Fuel}/n_{Air})_{st}} \tag{4}$$

$$\phi_{CH_4} = \frac{n_{CH_4}/n_{Air}}{(n_{Fuel}/n_{Air})_{st}} \tag{5}$$

The denominator of ϕ_{H_2} and ϕ_{CH_4} is the stoichiometric fuel/air molar ratio, and the numerator is the ratio of individual fuel to the amount of air available for its oxidation. Fig. 3 illustrates the equivalence ratio of hydrogen (ϕ_{H_2}) and methane (ϕ_{CH_4}) at different hydrogen percentages at the total equivalence ratio of 0.8. Since there are two fuels in the mixture, the Lewis number should be a weighed average value. In this study, as proposed by Law et al. [34], the Lewis number is evaluated from the following:

$$Le_{eff} = 1 + \frac{q_{H_2}(Le_{H_2} - 1) + q_{CH_4}(Le_{CH_4} - 1)}{q} \tag{6}$$

where the parameter q_i (i refers to H_2 and CH_4) is the nondimensional heat release associated with the consumption of species i, defined as

$$q_i = \frac{QY_i}{c_p T_u} \tag{7}$$

Here, Q is the heat of reaction, c_p is the unburned gas specific heat, T_u is the unburned gas temperature and Y_i is the supply mass fraction of species i. The quantity $q = q_{H_2} + q_{CH_4}$ is the total heat release and Le_{H_2} and Le_{CH_4} are the Lewis numbers of hydrogen–air mixture at ϕ_{H_2} and methane–air mixture at ϕ_{CH_4}, respectively.

3. Laminar burning velocity and Markstein length

For an outwardly propagating spherical flame, the stretched flame velocity, S_n, reflecting the flame propagation speed, is derived from the flame radius versus time [25]

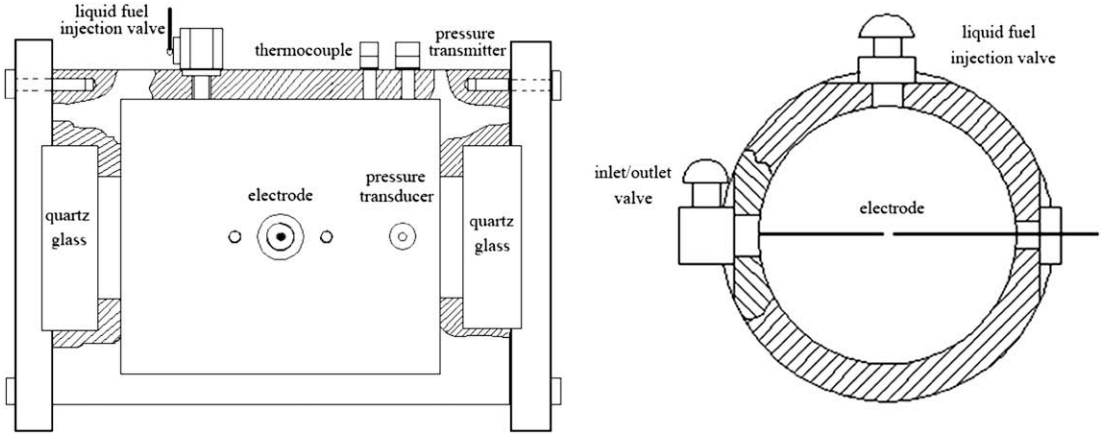

Fig. 2 – Schematic of constant volume combustion vessel.

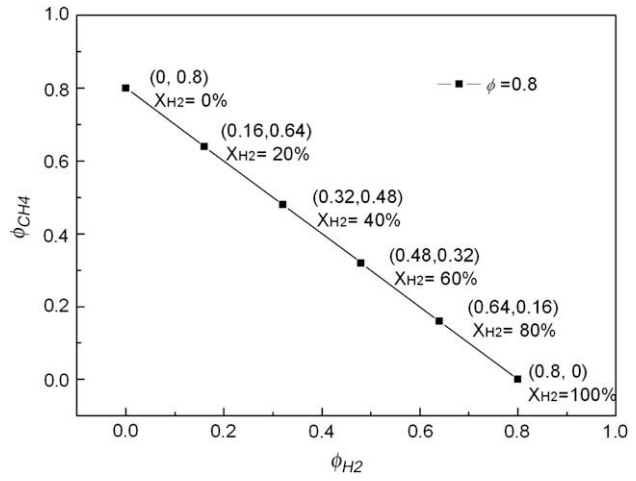

Fig. 3 – Methane based ϕ_{CH_4} and hydrogen based ϕ_{H_2} equivalence ratios at different hydrogen fractions.

$$S_n = \frac{dr_u}{dt} \tag{8}$$

where r_u is the radius of flame in Schlieren photograph and t is the elapsing time from spark ignition.

A general definition of stretch at any point on the flame surface is the Lagrangian time derivative of the logarithm of the area A of any infinitesimal element of the surface

$$\alpha = \frac{d(\ln A)}{dt} = \frac{1}{A}\frac{dA}{dt} \tag{9}$$

For the outwardly propagating spherical flame, the flame stretch rate can be deduced in the following form

$$\alpha = \frac{1}{A}\frac{dA}{dt} = \frac{2}{r_u}\frac{dr_u}{dt} = \frac{2}{r_u}S_n \tag{10}$$

In respect to the early stage of flame expansion, there exists a linear relationship between the flame speed and the flame stretch rate [18].

$$S_l - S_n = L_b\alpha \tag{11}$$

where S_l is the unstretched flame propagation speed, obtained as the intercept value of S_n at $\alpha = 0$ in the plot of S_n against α. Burned gas Markstein length L_b is the negative value of the slope of S_n–α curve.

The characteristics of the igniter can influence the measured value of burning velocity. Previous study showed that flame speeds were independent of ignition energy when flame radius was larger than 5 mm. This phenomenon was also observed by Bradley et al. [18], Lamoureux et al. [25] and Huang et al. [30]. To avoid the effect of ignition energy and pressure rise in the combustion chamber, the flame photos in the range of 5–25 mm were used in the analysis. Besides, because Eqs. (8)–(11) were used only for the smooth flame front, the measurements were also restricted before the occurrence of the cellular structure [35].

In the early stage of flame propagation, the flame undergoes an isobaric developing process, the unstretched laminar burning velocity, u_l, is related to S_l from mass conservation across the flame front

$$A\rho_u u_l = A\rho_b S_l \tag{12}$$

where A is the flame front area, ρ_u and ρ_b are the unburned and burned gas densities, respectively. The unstretched laminar burning velocity, u_l, can be obtained from Eq. (12)

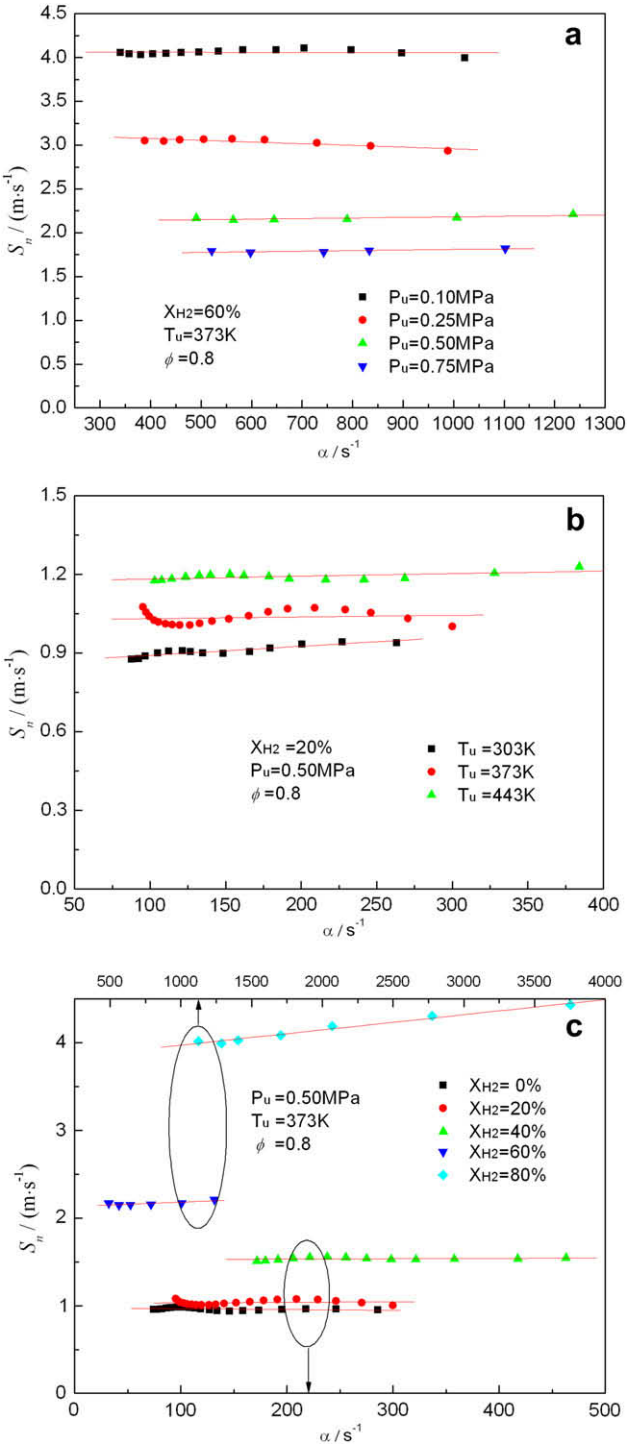

Fig. 4 – Flame propagation speed versus flame stretch rate at different initial pressures and initial temperatures for methane–hydrogen–air mixtures.

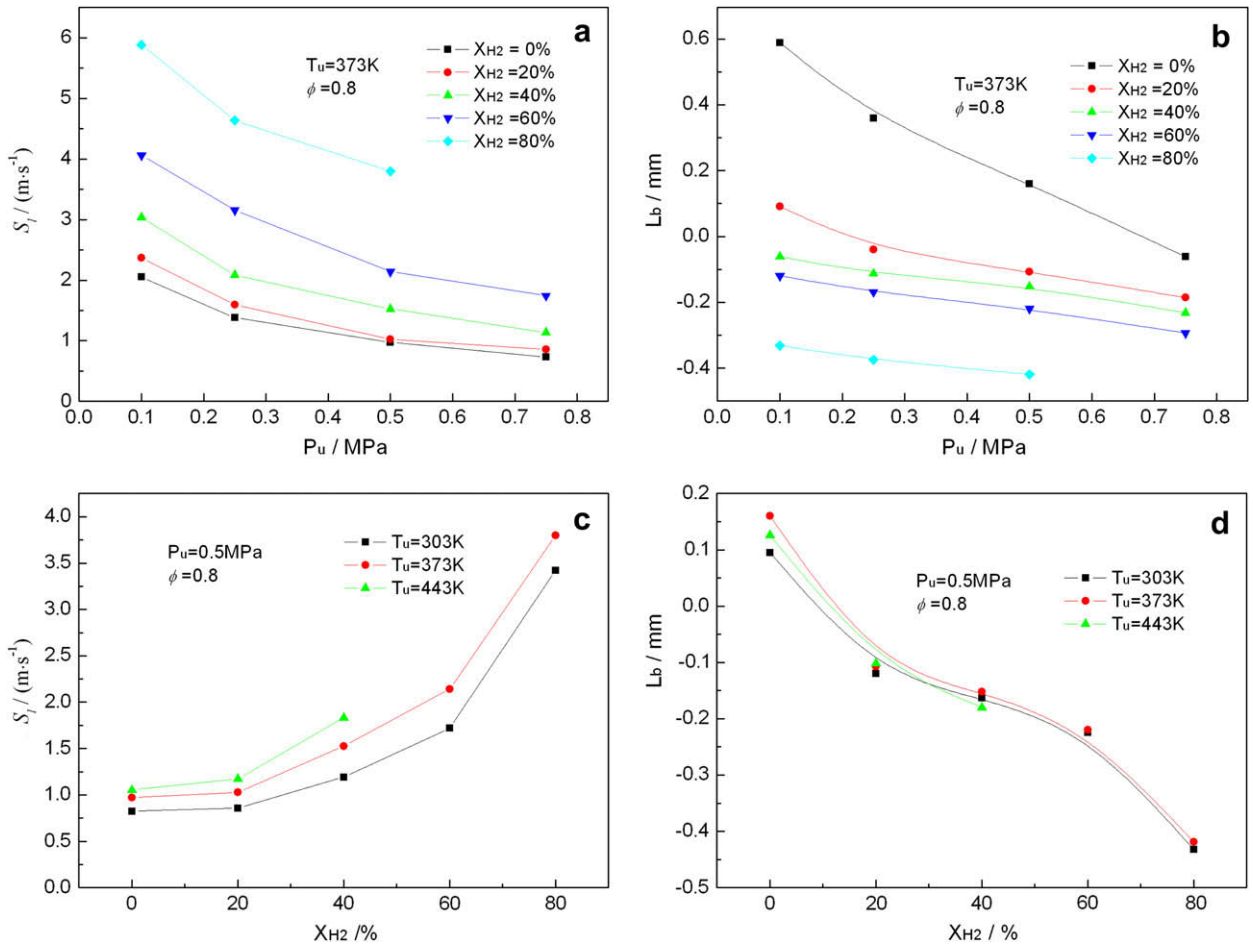

Fig. 5 – Unstretched flame propagation speed and Markstein length at different initial pressures and initial temperatures for methane–hydrogen–air mixtures.

$$u_l = \rho_b S_l / \rho_u \tag{13}$$

In this study, the laminar flame thickness, δ_l, is determined as [34,36]

$$\delta_l = \frac{D_{th}}{u_l}, \tag{14}$$

where D_{th} is thermal diffusivity of unburned gas, which is defined as

$$D_{th} = \frac{\lambda}{\rho_u c_p} \tag{15}$$

Here, λ and c_p are the thermal conductivity and specific heat of unburned gas, respectively.

4. Results and discussions

4.1. *Flame propagation velocity and Markstein length*

Fig. 4 shows the flame propagation speed versus flame stretch rate at an equivalence ratio of 0.8. In the early stage of flame propagation where the flame radius is small, the stretch rate of flame front surface is large. Removing the data affected by the ignition energy and electrodes during the early stage of flame development and large radius where pressure is increased, a linear correlation between the stretched flame propagation speed and the flame stretch rate is demonstrated. The unstretched flame propagation speed, S_l, is obtained as the intercept value of S_n at $\alpha = 0$ in the plot of S_n versus α. Importantly, this gives the value of laminar burning velocity u_l from Eq. (13). The flame propagation speed versus flame stretch rate for hydrogen percentage of 60% at initial temperature of 373 K and at different initial pressures is illustrated in Fig. 4a. The stretched flame propagation speeds decrease with the increase of stretch rate at all initial pressure conditions, and the gradients of S_n–α lines take the negative values, representing the positive values of Markstein length, L_b. Fig. 4b shows the flame propagation speed versus flame stretch rate at $P_u = 0.5$ MPa and $X_{H_2} = 20\%$ under different initial temperatures. Increasing the initial temperature from 303 K to 443 K shows little influence on flame stretch, but flame propagation speed increases with the increase of initial temperature. Fig. 4c shows the S_n–α curve for the mixtures with different hydrogen fractions at $P_u = 0.5$ MPa and $T_u = 373$ K. The results show that the stretched flame propagation speeds are increased and the burned gas Markstein lengths (L_b) are decreased with the increase of hydrogen

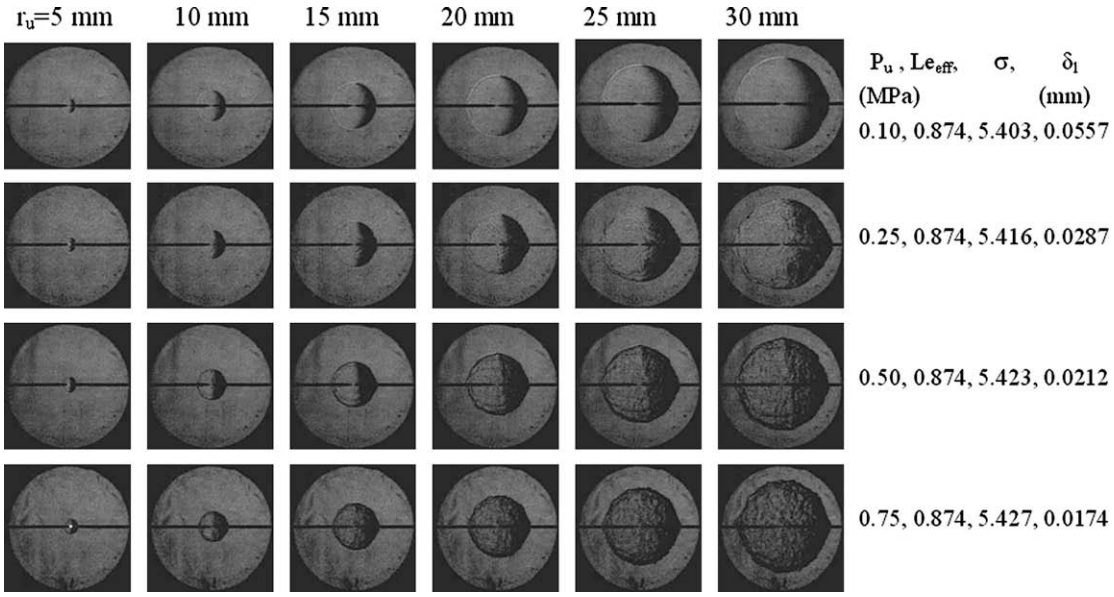

Fig. 6 – Schlieren images of methane–hydrogen–air mixtures at different initial pressures (X_{H_2} = 60%, T_u = 373 K).

fraction, and this indicates that the flame instability will be increased with the increase of hydrogen fraction.

Fig. 5 shows the unstretched flame propagation speed (S_l) and Markstein length (L_b) versus initial pressure and hydrogen fraction at an equivalence ratio of 0.8. As shown in Fig. 5a, the unstretched flame propagation speed is decreased with the increase of initial pressure. For a fixed initial pressure, the unstretched flame propagation speed is increased with the increase of hydrogen fraction. Variations of Markstein length (L_b) with initial pressure are illustrated in Fig. 5b. The results show that L_b is decreased with the increase of initial pressure, and this indicates the increase of flame front instability at the elevated pressure. Fig. 5c shows the S_l versus hydrogen fraction at different initial temperatures. S_l shows an exponent increasing trend with the increase of X_{H_2}. For a given hydrogen fraction, S_l is increased with the increase of initial temperature. Fig. 5d shows that L_b decreased remarkably with the increase of X_{H_2} and reveals the increase of flame front instability when hydrogen is added. With the increase of hydrogen fraction, the flame behavior tends to be similar to that of lean hydrogen flame, which is diffusional-thermally unstable. The study shows no appreciable difference in L_b at different initial temperatures.

4.2. *Flame stability and cellular structure*

Cellular flames tend to develop in the mixtures in which the deficient reactant constituent is also the constituent with the largest diffusivity. This kind of flame cellularity was experimentally observed for both the plane flame from the study of Markstein [37] and the spherically expanding flame from Manton et al. [38]. The formation of cells in such cases is a consequence of diffusional-thermal instability, which results from the competing effects of heat conduction from the flame and reactant diffusion toward the flame [39,40]. Lewis number (*Le*) is used to represent the instability and

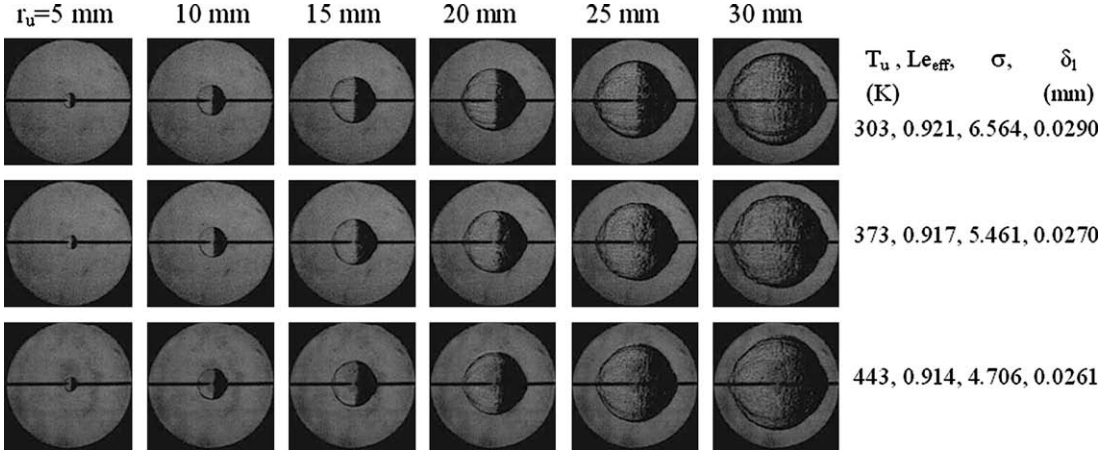

Fig. 7 – Schlieren images of methane–hydrogen–air mixtures at different initial temperatures (X_{H_2} = 40%, P_u = 0.5 MPa).

Lewis number is defined as the ratio of heat diffusivity of the mixture to mass diffusivity of the limiting reactant. When *Le* is below some critical value, *Le**(slightly lower than unity), the diffusional-thermal instability can be observed during the initial phase of propagation, i.e., the flame radius is the order of flame thickness [40]. On the other hand, mixtures with *Le* larger than unity are stable due to the diffusional-thermal mechanism. However, some experiments also observed the cellular flames in such cases [41–43]. This is regarded as the intrinsic Darrieus–Landau hydrodynamic instability resulting from the interaction of the flame with the hydrodynamic disturbances [40], and this instability is enhanced when the thermal expansion ratio (σ), which is the ratio of unburned gas to burned gas at two sides of the flame front, is increased and the flame thickness (δ_l) is decreased [20,27]. At the early stage of flame development, instability of flame is mainly influenced by thermo-diffusive factor. However, with flame development and flame radius increasing, the hydrodynamic factor becomes the dominant factor [27]. Initially, the cellular instability is suppressed by the strong curvature associated with small flame radii. As the flame expands and stretch lessens, there appears a critical radius (R_{cr}) where the cellular instability can no longer be suppressed, resulting in the instantaneous formation of cells over the entire flame surface. The transition position depends on the combined influence of the hydrodynamic and thermal-diffusive instabilities. Bechtold and Matalon [40] and Addabbo et al. [44] presented an explicit expression for the onset of cellularity by introducing a critical Peclet number (Pe_{cr}), which is the value of flame radius at transition or critical radius (R_{cr}), normalized by laminar flame thickness (δ_l).

Fig. 6 shows the Schlieren images of the expanding spherical flame at $T_u = 373$ K and at different pressures for methane–hydrogen–air mixtures. The flame front remains a smooth surface at an initial pressure of 0.1 MPa. At the elevated pressures, the flame surface first appears to be smooth, then some cracks grow and branch until eventually cellular structure appears over the entire flame surface. The onset of cellularity occurs at early position with the increase of initial pressure. The effective Lewis number (Le_{eff}) keeps the same value at different initial pressures for the fixed ϕ and X_{H_2}, as shown on the right side of Fig. 6, and this reveals little variation in diffusional-thermal instability with the increase of initial pressure. The hydrodynamic instability originated from gas thermal expansion (σ) and flame thickness (δ_l). The study shows that the thermal expansion ratio remains the same at different initial pressures, and the remaining parameter that governs the hydrodynamic instability is the flame thickness. Fig. 6 also lists the flame thickness, seen in the table attached on the right side of the figure. The increase in hydrodynamic instability with increasing initial pressure resulted from the decrease in flame thickness. The combined result of the two instabilities leads to the flame instability enhanced with the increase of initial pressure.

To identify the effect of initial temperature on the flame instability, the Schlieren images at different initial temperatures are provided in Fig. 7. The results show that flame instability is insensitive to the initial temperature. When initial temperature is increased, the flame instability shows little variations. The effective Lewis number (Le_{eff}) decreases slightly with the increase of initial temperature for the fixed ϕ and X_{H_2}, as shown on the right side of Fig. 7, and this

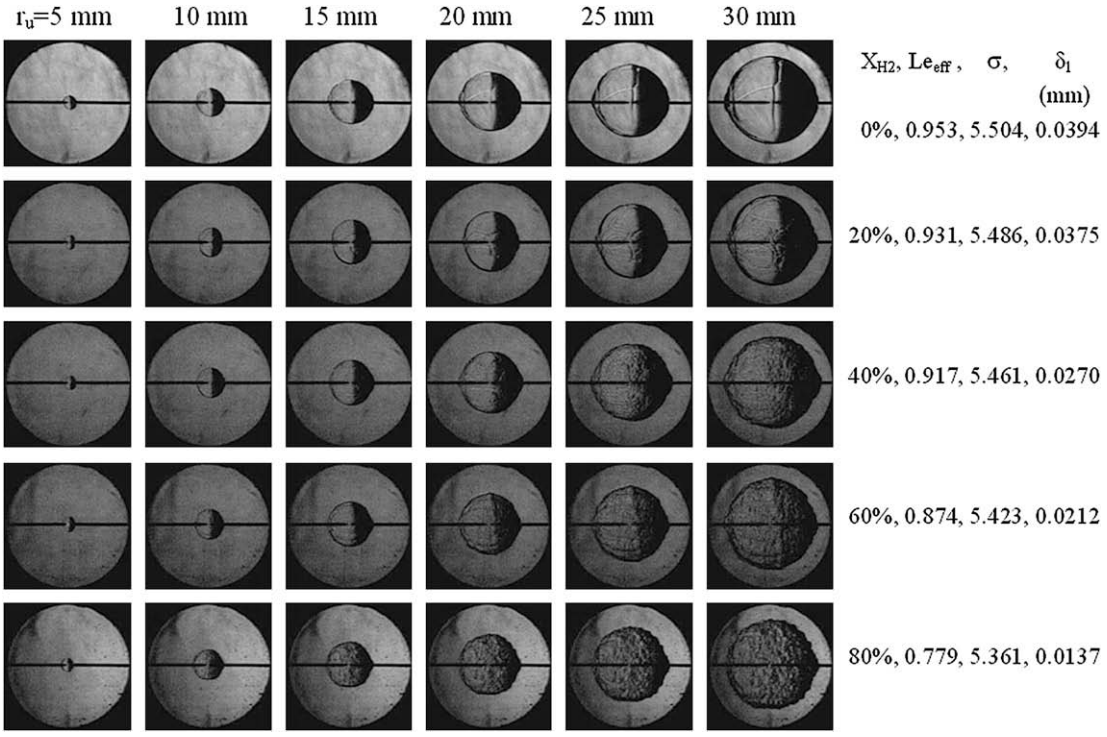

Fig. 8 – Schlieren pictures of methane–hydrogen–air mixtures at $P_u = 0.5$ MPa, $T_u = 373$ K and at various hydrogen fractions.

indicates that initial temperature has little influence on the diffusional-thermal instability. The values of thermal expansion (σ) and flame thickness (δ_l) at different initial temperatures are also provided on the right side of Fig. 7. With the increase of initial temperature, both σ and δ_l are decreased. The factor σ leads to the decrease of hydrodynamic instability while factor δ_l leads to the increase of hydrodynamic instability. The combined influence of the two factors results in little variation in flame front instability at different temperatures.

Fig. 8 shows the Schlieren images at different hydrogen fractions under the equivalence ratio of 0.8. No instabilities are observed for the methane–air flame ($X_{H_2} = 0\%$), although some cracks appear on the flame front surface, which are caused by the ignition disturbance. However, these cracks do not develop during the flame propagation. When hydrogen is added, flame instability can be observed, especially in large X_{H_2} cases. Earlier onset of cellular flame structure is presented at $X_{H_2} = 60\%$ compared to $X_{H_2} = 40\%$. With the increase of X_{H_2}, the effective Lewis number is decreased, indicating the increase of the diffusional-thermal instability. Flame becomes more similar to that of lean hydrogen–air flame at large hydrogen fraction, which is diffusional-thermally unstable [45]. In addition, the thermal expansion ratio gives little variation at different hydrogen fractions while the flame thickness is decreased significantly with the increase of hydrogen fraction, as shown in data on the right side of Fig. 8. Advance of the onset of cellular instability is from the thermal-diffusional instability as decreased Lewis number and the hydrodynamic instability as decreased laminar flame thickness. For methane–hydrogen–air flame, when X_{H_2} becomes large, both the diffusional-thermal instability and the hydrodynamic instability are enhanced, leading to the advancing onset of cellular flame.

Fig. 9 shows the stretched flame propagation speed versus flame radius at different initial pressures and hydrogen fractions. In the early stage of flame propagation, the value of S_n is decreased as the flame propagated and the Schlieren flame photos showed sign of cellularity. However, at certain positions as indicated by the asterisks, the flame front becomes cellular pattern and from this position S_n starts to increase remarkably due to the increase of the flame front area [36,46]. The flame radius of this position is defined as the critical radius, R_{cr}. When normalized by flame thickness, δ_l, it gives the critical Peclet number, Pe_{cr}, for the given conditions. Clearly, the value of R_{cr} is decreased when initial pressure and/or hydrogen fraction is increased.

To clearly illustrate the effect of cellular structure on flame propagation speed, Fig. 10 plots the stretched flame speed against the stretch rate. There is a rapid increase in S_n at critical flame radii. This transition point represents the onset of the cellular structure [32]. The information revealed from S_n versus α curve is consistent with the photo observed.

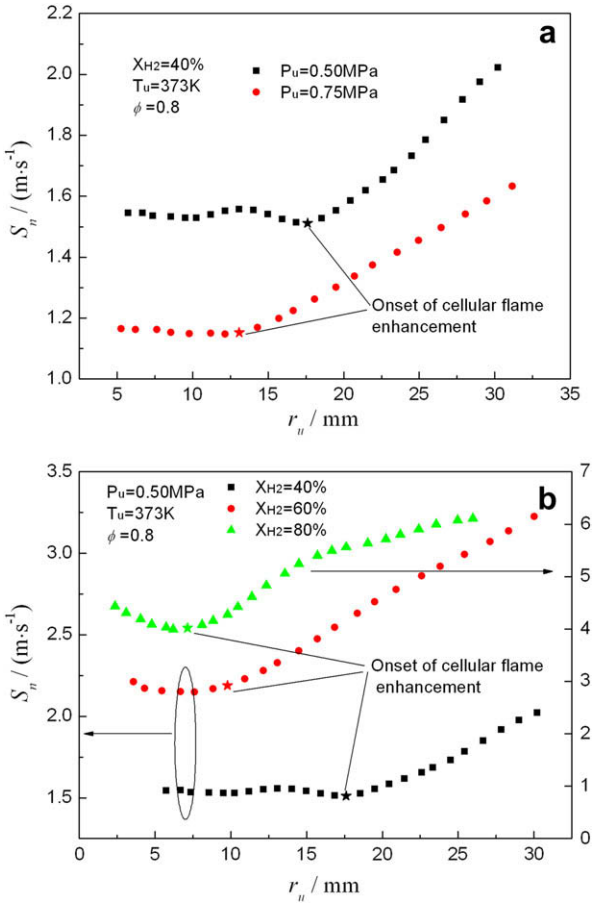

Fig. 9 – Stretched flame propagation speed versus flame radius.

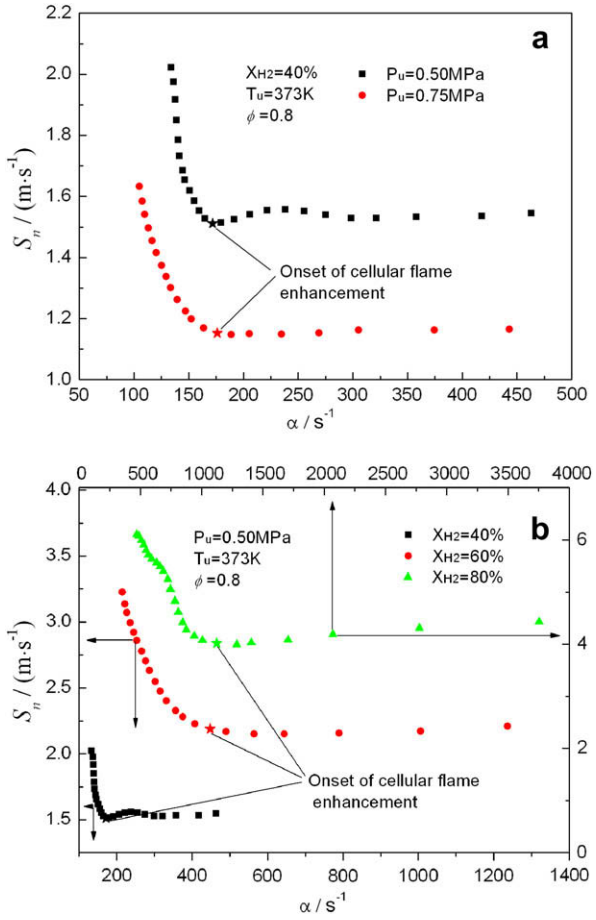

Fig. 10 – Stretched flame propagation speed versus stretch rate.

Fig. 11 shows the critical radius (R_{cr}) and critical Peclet number (Pe_{cr}) versus hydrogen fraction for methane–hydrogen–air mixtures. When X_{H_2} is less than 20%, no cellular instability is observed within the observed flame radius range. As X_{H_2} increases, both R_{cr} and Pe_{cr} are decreasing. For a fixed X_{H_2}, R_{cr} is decreased when initial pressure is increased. This indicates that the destabilizing effect will become stronger when increasing initial pressure and hydrogen fraction.

4.3. *Laminar burning velocity*

Fig. 12 shows the unstretched laminar burning velocity at different initial pressures and initial temperatures for lean methane–hydrogen–air flames. The unstretched laminar burning velocity is decreased monotonically with the increase of initial pressure and is increased with the increase of initial temperature. As the pressure is increased, the intensity of the temperature-sensitive, two body, branching reaction: $H + O_2 \rightarrow OH + O$ is approximately fixed due to the insensitivity of adiabatic temperature to the increase in pressure, while the three body, temperature-insensitive, inhibiting reaction: $H + O_2 + M \rightarrow HO_2 + M$ is enhanced, and a retarding effect is therefore imposed on the overall progress of the reaction with increasing pressure [19,47,48]. An increase in the upstream temperature leads to the increase of the adiabatic temperature, hence the reaction rate, and the dependence is more sensitive at high T_u because of the Arrhenius factor. u_l is increased with the increase of X_{H_2}, and the increasing trend becomes more obviously at larger X_{H_2}. Hydrogen addition increases the concentration of radicals from the activation reaction region where they are generated [13,49]. In addition, the volumetric heating value of hydrogen is lower than that of methane, but the fuel–air ratio of hydrogen is *four* times as that of methane at the stoichiometric condition. Thus, increasing hydrogen fraction decreases the amount of air in which nitrogen is a major component in determining the specific heat of the mixture, consequently resulting in the increase of adiabatic temperature and enhancing the reaction rate with the increase of hydrogen fraction.

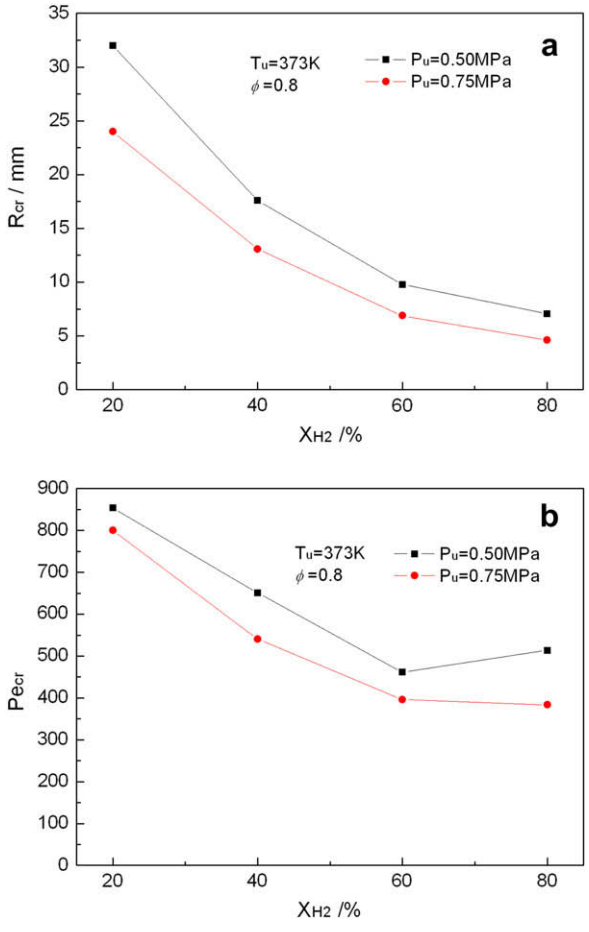

Fig. 11 – Critical radius and Peclet number versus X_{H_2} at different initial pressures and at different hydrogen fractions.

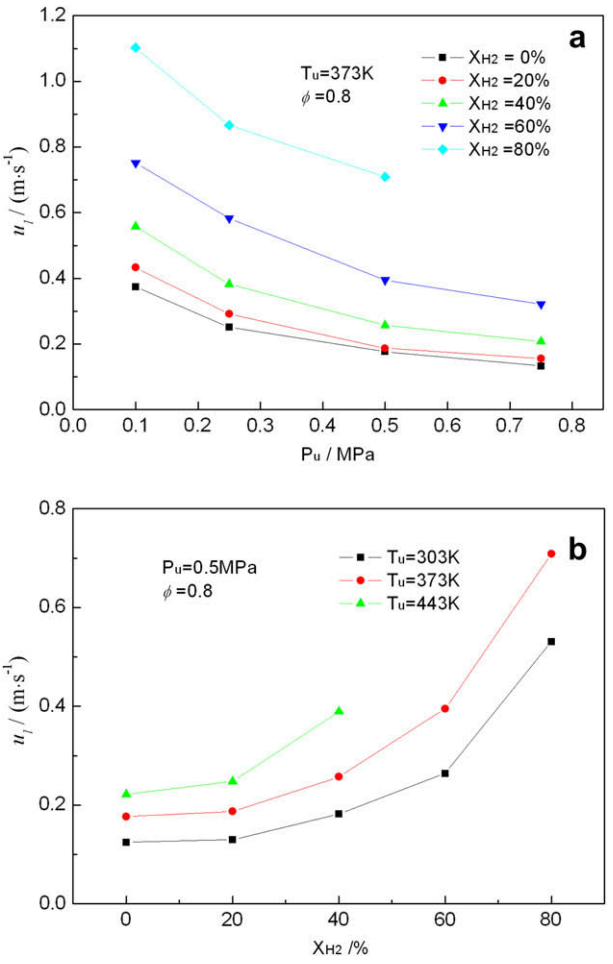

Fig. 12 – Laminar burning velocity (u_l) at different initial pressures and initial temperatures for methane–hydrogen–air mixtures.

5. Conclusions

An experimental study on laminar burning velocities and onset of cellular instabilities of methane–hydrogen–air

mixtures using the spherically expanding flames was conducted at different initial pressures, initial temperatures, and hydrogen fractions. The conclusions are summarized as follows.

(1) The unstretched flame propagation speed and the unstretched laminar burning velocity increase with the increase of initial temperature and hydrogen fraction, and they decrease with the increase of initial pressure.
(2) With the increase of initial pressure, advancement of onset of cellular instability is presented and the critical radius and Markstein length are decreased, indicating the increase of hydrodynamic instability with the increase of initial pressure. The initial temperature is insensitive to the flame instability.
(3) At the equivalence ratio of 0.8, significant decrease of critical radius and Markstein length with the increase of hydrogen fraction are presented, indicating the increase in both diffusional-thermal and hydrodynamic instabilities when hydrogen fraction is increased.

Acknowledgments

This study is supported by the National Basic Research Program of China (grant no. 2007CB210006) and by the National Natural Science Foundation of China (grant nos. 50636040 and 50821604).

REFERENCES

[1] Rousseau S, Lemoult B, Tazerout M. Combustion characteristics of natural gas in a lean burn spark-ignition engine. Proc Inst Mech Eng Part D J Automob Eng 1999; 213(D5):481–9.
[2] Ben L, Dacros NR, Truquet R, Charnay G. Influence of air/fuel ratio on cyclic variation and exhaust emission in natural gas SI engine. SAE Paper 992901; 1999.
[3] Ma FH, Wang Y, Liu HQ, Li Y, Wang JJ, Zhao SL. Experimental study on thermal efficiency and emission characteristics of a lean burn hydrogen enriched natural gas engine. Int J Hydrogen Energy 2007;32(18):5067–75.
[4] Ma FH, Liu HQ, Wang Y, Li Y, Wang JJ, Zhao SL. Combustion and emission characteristics of a port-injection HCNG engine under various ignition timings. Int J Hydrogen Energy 2008; 33(2):816–22.
[5] Ma FH, Wang Y, Liu HQ, Li Y, Wang JJ, Ding SF. Effects of hydrogen addition on cycle-by-cycle variations in a lean burn natural gas spark-ignition engine. Int J Hydrogen Energy 2008;33(2):823–31.
[6] Ma FH, Wang Y. Study on the extension of lean operation limit through hydrogen enrichment in a natural gas spark-ignition engine. Int J Hydrogen Energy 2008;33(4):1416–24.
[7] Hu EJ, Huang ZH, Liu B, Zheng JJ, Gu XL, Huang B. Experimental investigation on performance and emissions of a spark-ignition engine fuelled with natural gas–hydrogen blends combined with EGR. Int J Hydrogen Energy 2009;34(1): 528–39.
[8] Hu EJ, Huang ZH, Liu B, Zheng JJ, Gu XL. Experimental study on combustion characteristics of a spark-ignition engine fueled with natural gas–hydrogen blends combining with EGR. Int J Hydrogen Energy 2009;34(2):1035–44.
[9] Aung KT, Hassan MI, Faeth GM. Flame stretch interactions of laminar premixed hydrogen/air flames at normal temperature and pressure. Combust Flame 1997;109(1–2):1–24.
[10] Huzayyin AS, Moneib HA, Shehatta MS, Attia AMA. Laminar burning velocity and explosion index of LPG–air and propane–air mixtures. Fuel 2007;87(1):39–57.
[11] Milton BE, Keck JC. Laminar burning velocities in stoichiometric hydrogen and hydrogen–hydrocarbon gas mixtures. Combust Flame 1984;58(1):13–22.
[12] Vagelopoulos CM, Egolfopoulos FN. Direct experimental determination of laminar flame speeds. Proc Combust Inst 1998;27(1):513–9.
[13] Yu G, Law CK, Wu CK. Laminar flame speeds of hydrocarbon air mixtures with hydrogen addition. Combust Flame 1986; 63(3):339–47.
[14] Bosschaart KJ, de Goey LPH, Burgers JM. The laminar burning velocity of flames propagating in mixtures of hydrocarbons and air measured with the heat flux method. Combust Flame 2004;136(3):261–9.
[15] Bosschaart KJ, de Goey LPH. Detailed analysis of the heat flux method for measuring burning velocities. Combust Flame 2003;132(1–2):170–80.
[16] Tseng LK, Ismail MA, Faeth GM. Laminar burning velocities and Markstein numbers of hydrocarbon/air flames. Combust Flame 1993;95(4):410–26.
[17] Marley SK, Roberts WL. Measurements of laminar burning velocity and Markstein number using high-speed chemiluminescence imaging. Combust Flame 2005;141(4):473–7.
[18] Bradley D, Gaskell PH, Gu XJ. Burning velocities, Markstein lengths, and flame quenching for spherical methane–air flames: a computational study. Combust Flame 1996; 104(1–2):176–98.
[19] Sun CJ, Sung CJ, He L, Law CK. Dynamics of weakly stretched flames: quantitative description and extraction of global flame parameters. Combust Flame 1999;118(1–2):108–28.
[20] Gu XJ, Haq MZ, Lawes M, Woolley R. Laminar burning velocity and Markstein lengths of methane–air mixtures. Combust Flame 2000;121(1–2):41–58.
[21] Liao SY, Jiang DM, Gao J, Huang ZH. Measurements of Markstein numbers and laminar burning velocities for natural gas–air mixtures. Energy Fuels 2004;18(2):316–26.
[22] Hermanns RTE, Konnov AA, Bastiaans RJM, de Goey LP. Laminar burning velocities of diluted hydrogen–oxygen–nitrogen mixtures. Energy Fuels 2007;21(4):1977–81.
[23] Dowdy DR, Smith DB, Taylor SC, Williams A. The use of expanding spherical flames to determine burning velocities and stretch effects in hydrogen/air mixtures. Proc Combust Inst 1991;23(1):325–32.
[24] Kwon OC, Faeth GM. Flame/stretch interactions of premixed hydrogen-fueled flames: measurements and predictions. Combust Flame 2001;124(4):590–610.
[25] Lamoureux N, Djebäýli-Chaumeix N, Paillard CE. Laminar flame velocity determination for H_2–air–He–CO_2 mixtures using the spherical bomb method. Exp Therm Fluid Sci 2003; 27(4):385–93.
[26] Qiao L, Kim CH, Faeth GM. Suppression effects of diluents on laminar premixed hydrogen/oxygen/nitrogen flames. Combust Flame 2005;143(1–2):79–96.
[27] Law CK, Kwon OC. Effects of hydrocarbon substitution on atmospheric hydrogen–air flame propagation. Int J Hydrogen Energy 2004;29(8):867–79.
[28] Miller DR, Evers RL, Skinner GB. Effects of various inhibitors on hydrogen–air flame speeds. Combust Flame 1963;7(1): 137–42.
[29] Liu Y, Lenze B, Leuckel W. Investigation on the laminar and turbulent burning velocities of premixed lean and rich

flames of methane–hydrogen–air mixtures. Prog Astronaut Aeronaut 1991;131(3):259–74.
[30] Huang ZH, Zhang Y, Zeng K, Liu B, Wang Q, Jiang DM. Measurements of laminar burning velocities for natural gas–hydrogen–air mixtures. Combust Flame 2006;146(1–2):302–11.
[31] Ren JY, Qin W, Egolfopoulos FN, Tsotsis TT. Strain-rate effects on hydrogen-enhanced lean premixed combustion. Combust Flame 2001;124(4):717–20.
[32] Ren JY, Qin W, Egolfopoulos FN, Mak H, Tsotsis TT. Methane reforming and its potential effect on the efficiency and pollutant emissions of lean methane–air combustion. Chem Eng Sci 2001;56:1541–9.
[33] Halter F, Chauveau C, DjebaIli-Chaumeix N, Gokalp I. Characterization of the effects of pressure and hydrogen concentration on laminar burning velocities of methane–hydrogen–air mixtures. Proc Combust Inst 2005;30(1):201–8.
[34] Law CK, Jomaas G, Bechtold JK. Cellular instabilities of expanding hydrogen/propane spherical flames at elevated pressures: theory and experiment. Proc Combust Inst 2005;30(1):159–67.
[35] Bradley D, Lawes M, Liu Kexin, Verhelst S, Woolley R. Laminar burning velocities of lean hydrogen–air mixtures at pressures up to 1.0 MPa. Combust Flame 2007;149(1–2):162–72.
[36] Law CK, Sung CJ. Structure, aerodynamics, and geometry of premixed flamelets. Prog Energ Combust 2000;26(4–6):459–505.
[37] Markstein GH. Cell structure of propane flames burning in tubes. J Chem Phys 1949;17(4):428–9.
[38] Manton J, von Elbe G, Lewis B. Nonisotropic propagation of combustion waves in explosive gas mixtures and the development of cellular flames. J Chem Phys 1952;20(1):153–7.
[39] Parlange JY. Influence of preferential diffusion on the stability of a laminar flame. J Chem Phys 1968;48(4):1843–9.
[40] Bechtold JK, Matalon M. Hydrodynamic and diffusion effects on the stability of spherically expanding flames. Combust Flame 1987;67(1):77–90.
[41] Groff EG. The cellular nature of confined spherical propane–air flames. Combust Flame 1982;48:51–62.
[42] Bradley D, Harper CM. The development of instabilities in laminar explosion flames. Combust Flame 1994;99(3–4):562–72.
[43] Kwon OC, Rozenchan G, Law CK. Cellular instabilities and self-acceleration of outwardly propagating spherical flames. Proc Combust Inst 2002;29(2):1775–83.
[44] Addabbo R, Bechtold JK, Matalon M. Wrinkling of spherically expanding flames. Proc Combust Inst 2002;29(2):1527–35.
[45] Hu EJ, Huang ZH, He JJ, Jin C, Miao HY, Wang XB. Measurement of laminar burning velocities and analysis of flame stabilities for hydrogen–air–diluent premixed mixtures. Chin Sci Bull 2009;54(5):846–57.
[46] Bradley D, Hicks RA, Lawes M, Sheppard CGW, Woolley R. The measurement of laminar burning velocities and Markstein numbers for iso-octane–air and iso-octane–*n*-heptane–air mixtures at elevated temperatures and pressures in an explosion bomb. Combust Flame 1998;115(1–2):126–44.
[47] Sun CJ, Sung CJ, Hun DL, Law CK. Response of counterflow premixed and diffusion flames to strain rate variations at reduced and elevated pressures. Proc Combust Inst 1996;26(1):1111–20.
[48] Egolfopoulos FN, Law CK. Chain mechanisms in the overall reaction orders in laminar flame propagation. Combust Flame 1990;80(1):7–16.
[49] Jinhua Wang, Zuohua Huang, Chenglong Tang, Haiyan Miao, Xibin Wang. Numerical study of the effect of hydrogen addition on methane-air mixtures combustion. Int J Hydrogen Energy 2009;34(2):1084–96.